



Unraveling quantum dephasing of nitrogen-vacancy center ensembles in diamond



Jixing Zhang¹✉, Cheuk Kit Cheung¹, Michael Kübler¹, Magnus Benke¹, Mathis Brossaud², Yihua Wang¹, Andrej Denisenko¹, Ruoming Peng¹, Jens Anders³, Emilio Corcione⁴, Cristina Tarín Sauer⁴, Andrew M. Edmonds⁵, Matthew Markham⁵, Kazuo Nakamura^{6,12}, Hitoshi Sumiya⁷, Shinobu Onoda⁸, Junichi Isoya⁹, Chen Zhang¹⁰✉ & Jörg Wrachtrup^{1,11}

Nitrogen-vacancy (NV) center ensembles in diamond are one of the most promising solid-state quantum platforms for various sensing applications. Achieving ultimate sensitivity requires simultaneously long spin dephasing times (T_2^*) and high NV center concentrations. In this work, we propose a systematic measurement approach to quantify the electron spin dephasing in NV center ensembles and analyze the contributions of various sources to the dephasing time, including NV-NV interactions, strain and electric field distributions, ^{13}C nuclear spins, and P1 electron spins. Our method is validated using a series of high-performance diamond samples, providing a comprehensive understanding of dephasing mechanisms and revealing correlations between NV concentration and different dephasing sources. Building on these insights, we outline strategies to further enhance the achievable sensitivity for DC magnetic field measurements.

Over the past two decades, defects in solid state materials have been extensively studied as spin systems for quantum technologies^{1–3}. Among all known defects, the negatively charged nitrogen-vacancy (NV) center in diamond is one of the most promising platforms for various quantum applications^{4–7}. Compared to quantum sensors that have demonstrated ultrahigh sensitivity in applications such as magnetoencephalography (MEG)⁸, magnetometry based on NV centers in diamond is superior in applications that require high spatial resolution and small sensor volumes. For example, techniques that use a single NV center near the diamond surface or at a diamond tip can probe nanoscale magnetization to recognize the structure of protein molecules and 2D materials^{9–11}. Recently, it is also proposed to use NV centers to detect the unconventional charge-density-wave in Kagome materials¹². Beyond the nanometer scale, diamond magnetometry with spatial resolution in the range of micrometers to millimeters with high sensitivity¹³ is considered a potential technique for applications in magnetic imaging¹⁴, for example, in search of axions¹⁵.

The moderate sensitivity of NV ensemble magnetometry remains a major obstacle for practical applications¹⁶. A sensitivity approaching or better than $1 \text{ pT}/\sqrt{\text{Hz}}$ requires careful trade-off between defect concentration and the dephasing time T_2^* of the NV center ensembles¹⁷. The typical dephasing rate $\Gamma_2^* = 1/T_2^*$ of NV center ensembles ranges from tens of kHz up to several MHz, while the defect density ranges from 10^{16} cm^{-3} to 10^{18} cm^{-3} . For reference, a fT/ $\sqrt{\text{Hz}}$ level atomic magnetometer has atomic vapor with a density of approximately 10^{14} cm^{-3} while the decoherence rate is a few Hz¹⁹. Given the typically high defect density in diamonds, understanding the dephasing mechanisms of NV center ensembles is crucial to extending the coherence time in applications that require both high sensitivity and spatial resolution. This understanding will also enable the optimization of diamond growth and defect treatment processes, thereby advancing magnetometer performance^{18,20}. Furthermore, the NV center ensemble as a quantum many-body system offers a suitable framework to probe quantum thermodynamics and simulation, in which the unraveling of dephasing sources is fundamentally important^{21–23}. Additionally, it is also

¹3rd Institute of Physics, University of Stuttgart, Stuttgart, Germany. ²Université Paris-Saclay, ENS Paris-Saclay, DER de Physique, Gif-sur-Yvette, France.

³Institute of Smart Sensors, University of Stuttgart, Stuttgart, Germany. ⁴Institute for System Dynamics, University of Stuttgart, Stuttgart, Germany. ⁵Element Six Global Innovation Centre, Fermi Avenue, Harwell Oxford, Didcot, UK. ⁶Hydrogen & Carbon Management Technology Strategy Dept., Tokyo Gas Co., Ltd., Yokohama, Japan. ⁷Advanced Materials Laboratory, Sumitomo Electric Industries, Ltd., Itami, Japan. ⁸Quantum Materials and Applications Research Center, National Institutes for Quantum Science and Technology, Takasaki, Japan. ⁹Institute of Pure and Applied Sciences, University of Tsukuba, Tsukuba, Japan.

¹⁰Beijing Quantum Technology Research and Development Center, Beijing, China. ¹¹Max Planck Institute for Solid State Research, Stuttgart, Germany. ¹²Present address: Engineering Division, TsubameBHB Co., Ltd., Yokohama, Japan. ✉e-mail: jixing.zhang@pi3.uni-stuttgart.de; chen.zhang@cquaterd.cn

beneficial for the ab initio studies of the NV-related systems with the microscopic insights into the electronic correlations and hyperfine interactions^{24,25}.

Previous studies have focused on identifying the primary dephasing sources in specific diamond samples. For samples containing abundant paramagnetic spin defects, experimental studies combined with theoretical modeling have investigated the spin bath-induced decoherence, which enables the determination of paramagnetic spin concentrations^{26–30}. In addition, linewidth broadening induced by electric fields and strain in diamonds is investigated by optically detected magnetic resonance (ODMR) and interferometry methods^{31,32}. Studies have also addressed NV-NV interactions in diamonds with high-concentration NV centers^{21,33}. Due to the influence of multiple factors, the dephasing rate of NV center ensembles varies considerably across samples, resulting in diverse quantum sensing performances. However, isolating and quantifying the individual contributions of these dephasing mechanisms remains a significant technical challenge.

In this work, we present a comprehensive study using multiple experimental techniques that identify the dephasing mechanisms of NV ensembles in a series of high-quality diamonds under ambient conditions. Our methodology enables systematic characterization of key diamond properties, including electric field and strain distributions, nuclear and electron spin bath properties, and NV center densities. We applied this methodology to characterize diamond samples with varying NV concentrations. This enabled us to verify the relationships among electric field strength, Hahn Echo-measured decoherence rates, and NV concentration, while evaluating existing models that describe how different sources contribute to the total dephasing rate. Based on these findings, we investigate the fundamental DC sensitivity limit of the NV ensemble magnetometry and propose practical strategies to extend the coherence time T_2^* , providing a pathway towards further enhancing the magnetometer performance.

Results

A brief overview on dephasing mechanisms

We consider a simplified ground-state Hamiltonian for an ensemble of N NV centers, given by

$$\mathcal{H}_{NV} = \sum_{i=1}^N (D_{gs} + \delta^i) S_z^{i2} + \gamma_e \vec{B}_0 \cdot \vec{S}^i + A^i S_z^i + \sum_{i \neq j} \vec{S}^i \cdot V_{dd} \cdot \vec{S}^j. \quad (1)$$

Here, $D_{gs} = 2.87\text{GHz}$ denotes the zero-field-splitting (ZFS), δ^i accounts for the combined effects of local electric fields and strain at each NV center, γ_e is the electron gyromagnetic-ratio, \vec{B}_0 is the magnetic field, A^i denotes the average coupling strength arising from the spin bath (including both electron and nuclear spins), V_{dd} is the dipole-dipole interaction matrix between two NV centers. In the experiments, a magnetic field $\vec{B}_0 \approx 10\text{G}$ is applied along one NV axis (on-axis orientation), while its projections on the other three axes (off-axis orientations) are identical. As the bias field dominates over the perpendicular components, the latter are neglected in the equation.

Except for the second term (the Zeeman term), all other terms contribute to the dephasing of NV center ensembles. These dephasing-related terms can be classified into two groups. The first group - the inhomogeneous broadening - includes δ^i and A^i , which induce disorder among the NV centers. Specifically, δ^i arises from inhomogeneous strain distributions and in situ electric-field noise, while A^i originates from the nuclear spin bath (associated with ^{13}C) and the electron spin bath due to paramagnetic defects, such as P1 centers. The second group - homogeneous broadening - is dominated by NV-NV interactions, as represented by the last term in Eq. (1).

We assume that the dephasing sources are independent and result in an exponential decay. Thus, the dephasing rate of NV center ensembles can be

expressed as a summation model¹⁷:

$$\Gamma_2^* \approx \Gamma_{\text{strain}} + \Gamma_{\text{elec}} + \Gamma_{^{13}\text{C}} + \Gamma_{\text{P1}} + \Gamma_{\text{NV-NV}} + \Gamma_{\text{other}} + \Gamma_1. \quad (2)$$

Here, each term on the right-hand side represents the dephasing rate contributed by the corresponding mechanisms described above. The term Γ_{other} encompasses all dephasing sources not included in the primary mechanisms. At room temperature, T_1 for single NV centers is typically around 6 ms, which sets an upper bound on T_2^* and can therefore be neglected in this work³⁴. We also measured T_1 for all ensemble samples and found values consistent with this reference, except for those with the highest NV concentrations, where T_1 is slightly reduced (3 ms). Even in these cases, the corresponding relaxation rates remain well below the kilohertz level and are negligible compared to Γ_2^* . In the following subsections, we describe the methods employed to investigate each dephasing source individually. A specific sample is used as an example to demonstrate precise measurements of the dephasing rates in the subsequent sections.

Strain and electric field noise

The strain distribution in diamonds is inherently inhomogeneous due to imperfections in material fabrication. Similarly, the local electric field experienced by the NV centers is inhomogeneous, caused by the random spatial distribution of charged defects around the spins. Both effects modify the local potential experienced by the NV electrons, leading to shifts in the ground-state zero-field splitting. Consequently, both effects manifest as quadratic terms in the Hamiltonian, represented by δ^i in Eq. (1) (details are provided in the supplementary). Given that the magnetic dipole effect is linear, experimental sequences can be designed to selectively probe quadratic or linear terms by applying two microwave fields resonant with the $|0\rangle \rightarrow |+1\rangle$ and $|0\rangle \rightarrow |-1\rangle$ transitions, respectively. To isolate these contributions, we employ two complementary experimental protocols: the double quantum (DQ) Ramsey sequence and the strain-CPMG sequence^{32,35}, as illustrated in Fig. 1(a).

The DQ Ramsey sequence is insensitive to quadratic (S_z^2) terms but twice as sensitive to linear (S_z) terms compared to the conventional Ramsey sequence. Accordingly, $\Gamma_{\text{DQ}}/2$ provides a direct measure of dipolar-induced dephasing. In contrast, the strain-CPMG sequence implements a coherent state swap between $|+1\rangle$ and $|-1\rangle$, rendering it sensitive to quadratic terms while largely insensitive to linear contributions.

Moreover, $\Gamma_{\text{strain-cpmg}}$ incorporates contributions from Γ_2 , which can be estimated by Hahn-echo measurements. Summarizing these relationships, we obtain

$$\Gamma_{S_z^2} = \Gamma_{\text{strain}} + \Gamma_{\text{elec}} = \Gamma_{\text{strain-cpmg}} - \Gamma_2 \approx \Gamma_2^* - \Gamma_{\text{DQ}}/2, \quad (3)$$

where $\Gamma_{S_z^2}$ represents the dephasing rate induced by the S_z^2 term in \mathcal{H}_{NV} .

In Fig. 1b, measurements on the example sample yield $\Gamma_2^* = 137\text{kHz}$, $\Gamma_{\text{DQ}} = 216\text{kHz}$, $\Gamma_2 = 10\text{kHz}$, and $\Gamma_{\text{strain-cpmg}} = 60\text{kHz}$. From these results, it is evident that the total dephasing rate Γ_2^* is only an approximate summation of the dephasing contributions from the S_z and S_z^2 terms, rather than precisely in agreement with Eq. (3). This discrepancy can be attributed to simplifications in the summation dephasing model. The validity of this model is further examined in the discussion section with more samples.

To further distinguish the dephasing rates contributed by strain and electric fields, it is essential to account for the transverse components induced by strain and electric fields, which are neglected in Eq. (1). The parallel and perpendicular terms of the quadratic spin terms in the NV Hamiltonian, caused by isotropic strain and electric field noise, are not equivalent. Notably, the transverse electric dipole moment of the electric field results in a dip in the zero-field ODMR spectrum³¹, as shown in Fig. 1c. Because of the hyperfine splitting associated with the ^{14}N nuclear spin ($I = 1$), this effect is suppressed for the $|m_I = \pm 1\rangle$ transitions, and only the $|m_I = 0\rangle$ line exhibits a pronounced dip. The fitted linewidth of this dip, measured from the zero-field ODMR spectrum of the example sample, is approximately $\nu_{\text{zf-ODMR}} = 220\text{kHz}$. The dephasing rate induced by the

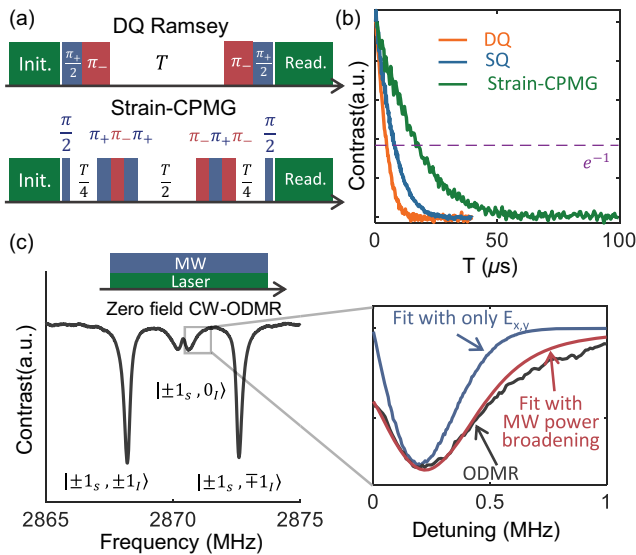


Fig. 1 | Distinguishing strain- and electric-field-induced dephasing in NV ensembles. **a** Double quantum Ramsey sequence (upper) and strain-CPMG sequence (lower). **b** Dephasing rate measurements from the example sample. **c** Zero-field ODMR spectrum, with an inset of the enlarged hyperfine line corresponding to the $|m_l = 0\rangle$ state. The line is fitted by considering both strain distribution and microwave power broadening.

electric field is determined as $\Gamma_{\text{elec}} = v_{\text{zf-ODMR}} \cdot d^{\parallel}/d^{\perp} = 4.5\text{kHz}$, where $d^{\parallel} = 0.35\text{ \AA} \cdot \text{cm/V}$ and $d^{\perp} = 17\text{ \AA} \cdot \text{cm/V}$ are the longitudinal and transverse parameters of the electric dipole moments. The dephasing rate introduced by the strain distribution is then estimated as $\Gamma_{\text{strain}} = \Gamma_{S_2^*} - \Gamma_{\text{elec}}$.

Dipolar noise from the spin bath

Dipolar noise from the spin bath significantly contributes to the dephasing of NV center ensembles. Randomly distributed electron and nuclear spins around the NV centers create distinct local magnetic fields at each NV center. Consequently, the spin bath induces a global exponential decay, with a rate proportional to the concentration of bath spins, due to variations in the energy splitting of individual NV centers. The contribution of the spin bath to the dephasing rates can be estimated using mean-field theory (details in the Supplementary)³⁶. Accordingly, the dephasing rate induced by the spins is linearly proportional to the spin density, allowing the estimation of spin concentrations from measured dephasing rates, and vice versa.

The contribution of the ¹³C nuclear spin bath to the dephasing rate is first estimated. Using the mean-field model (See Supplementary for details), the contribution of ¹³C (gyromagnetic ratio $\gamma_C = 10.7\text{ MHz/T}$) per unit density is derived as $\Gamma_{13C} = 0.1\text{ kHz/ppm}$. The example sample is isotopically purified to 0.03% ¹³C, corresponding to a concentration of 300 ppm. Hence, $\Gamma_{13C} = 30\text{ kHz}$. For diamonds with a natural abundance of ¹³C (1.1%), the ¹³C-induced dephasing rate is approximately 1.1 MHz. Consequently, the T_2^* of non-isotopically-purified diamonds is typically shorter than 1 μs , which primarily limits the sensitivity. Besides ¹³C, contributions from other nuclear spins (mostly ¹⁴N nuclear spins associated with defects such as P1 centers) can be neglected due to their low concentration.

With the ¹²C enriched diamonds, the primary spin bath source shifts to the electron spin bath, predominantly arising from unpaired electrons of substituted nitrogen atoms (P1 centers) in the lattice. Double electron-resonance (DEER) measurements are used to estimate the influence of electron spins (P1 centers^{29,33,37,38} and other dark spins³⁹) on dephasing. As shown in Fig. 2a, the DEER spectrum reveals the resonance peaks corresponding to all bath spins within the bandwidth. In the example, a 9.5 Gauss magnetic field is applied. The peaks correspond to multiple transitions arising from the rich energy-level structure. Details on the derivation of transition lines are provided in the Supplementary. An RF

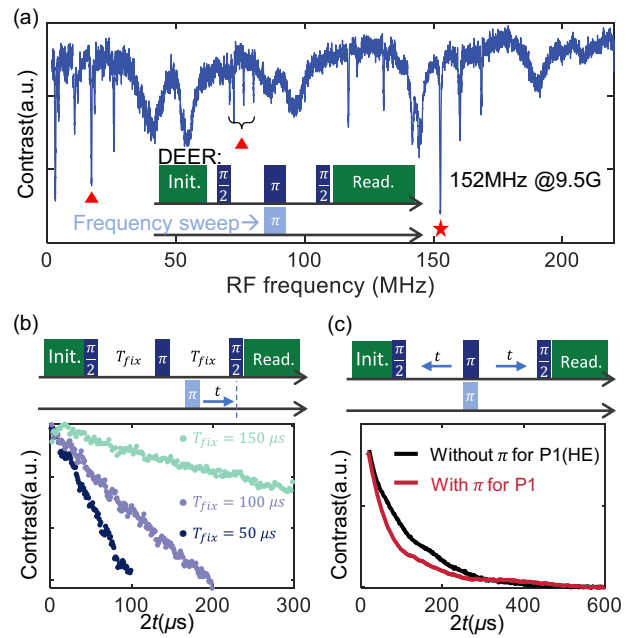


Fig. 2 | Characterization of spin-bath-induced dephasing using DEER measurements. **a** Measured DEER spectrum at a 9.5 Gauss magnetic field. The peaks marked by triangles are related to the dark spin transitions which do not belong to P1 center, while other peaks are P1 center related. The peak marked by a star is used in measurement in (b) and (c). **b** Pulse-sweep DEER sequence and the corresponding measured signals with the example sample. **c** Duration-sweep DEER sequence and the corresponding measured signals from the same sample.

pulse, tuned to the frequency of a specific resonance peak in the DEER spectrum, is applied during the Hahn-echo measurement, as shown in Fig. 2b and 2c, to characterize the dephasing caused by bath spins and estimate their concentrations. The resonance peak marked with a star in Fig. 2a is selected for this example sample to demonstrate the measurement process.

In the pulse-sweep DEER measurement illustrated in Fig. 2b, the signal decay follows the expression $\exp(-k_{\text{HE}} T_{\text{fix}}) \exp(-k_{nm} t)$, where k_{nm} represents the decay rate corresponding to the transition line of P1 from the n th state to the m th state. However, the experimental results exhibit linearly decaying signals rather than exponential decays. This behavior arises from the relatively low concentration of P1 centers, which results in $\Gamma_{P1} < \Gamma_2$ and restricts the interval T_{fix} of the sequence to the T_2 limit in pulse-sweep DEER. As a result, only the initial P1-induced decay curve is observable in the displayed results, appearing as an approximate linear decay. Consequently, the pulse-sweep DEER measurement is unsuitable for identifying the electron spin bath decay in high-quality diamond samples with low concentrations of paramagnetic defects.

To address the limitations of pulse-sweep DEER measurements, we propose using a duration-sweep DEER sequence, as illustrated in Fig. 2c. The signal decay follows $\exp(-(\Gamma_{P1, \text{DEER}} + \Gamma_2)t)$, enabling the sequence to determine the decay contribution of P1 centers, even at low concentrations. For the example sample, $\Gamma_{P1, \text{DEER}} + \Gamma_2 = 12.9\text{ kHz}$ is measured using the sequence with the DEER RF pulse, while $\Gamma_2 = 9.5\text{ kHz}$ is obtained using the sequence without it, yielding $\Gamma_{P1, \text{DEER}} = 3.4\text{ kHz}$ as the estimated dephasing rate of Γ_{P1} .

Typically, the mix of eigenstates of P1 centers is suppressed at a high magnetic field (>100 Gauss) so that the DEER measurement results follow a general mean-field theory³⁰. However, in most practical applications, including this work, the magnetic fields are relatively weak. Thus, the model is adjusted to account for the altered eigenstates of P1 centers under weak magnetic fields (see the Supplementary), and the relationship between Γ_{P1} and $\Gamma_{P1, \text{DEER}}$ is recalibrated, yielding $\Gamma_{P1} = 6\Gamma_{P1, \text{DEER}} = 20.4\text{ kHz}$. The dependence of Γ_{P1} on the P1 concentration is recalibrated for weak magnetic

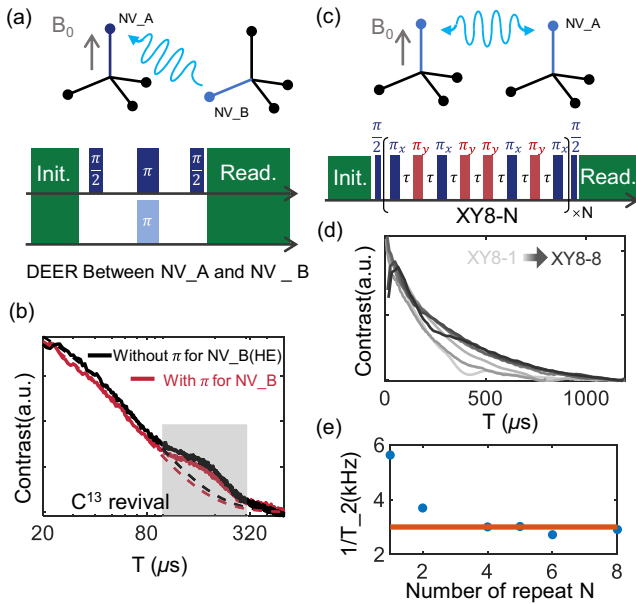


Fig. 3 | Measurement of NV-NV dipolar interactions in NV center ensembles. **a** Interaction between NV centers of different groups and the sequence for the corresponding DEER measurement. **b** Decay rate data (red) obtained using the DEER sequence, with Hahn-Echo results (black) shown for comparison. **c** Interaction between NV centers of the same group and the XY8- N sequence for the $\Gamma_{\text{NV-NV}}$ measurement. **d** Dephasing measurement using XY8- N sequences with different repetition numbers N . **e** Dependence of the dephasing rate on the repetition number N^n .

fields.(see the Supplementary). Moreover, additional peaks not corresponding to P1 transitions are observed in the DEER spectrum, as illustrated in Fig. 2a. The lines possibly originate from dark spins associated with various defects^{40,41}. In the example sample, the dephasing contribution from these spins is minimal. Additionally, the DEER spectra of P1 centers and other dark spins provide critical information for spin-bath driving, as shown in the Supplementary^{35,42–44}.

Dipole–dipole interactions among NV centers

In most cases, the contribution of dipole-dipole interactions among NV centers to dephasing is relatively small compared to other dephasing sources. Nevertheless, accurately measuring this contribution is still important, especially for the extension of T_2^* in samples containing high concentrations of NV centers and low concentrations of other defects³³. Furthermore, NV center concentrations can be precisely estimated by accurately measuring the NV-NV interaction. Together, these factors—extended T_2^* and precise NV concentration estimation—enable further optimization of the sensitivity of diamond magnetometry.

Diamond samples typically contain NV centers aligned along all four crystal orientations. We thus need to consider interactions both between NV centers along different orientations (off-axis) and interactions of NV centers along the same axis (on-axis). Similarly to the experiments in Section II C, a modification of the DEER sequence (with the P1-driving RF pulse replaced by the microwave pulse) can be used to investigate the strength of off-axis NV-NV interactions, as illustrated in Fig. 3a. For the example sample, the measured additional decay rate induced by off-axis NV interactions is $\Gamma_{\text{NV-off}} = 1.2\text{kHz}$ (Fig. 3b), corresponding to an NV⁻ concentration of 0.12ppm. However, certain limitations need to be addressed in practical applications, as outlined below. Firstly, imperfections in the microwave π pulse can reduce the dephasing in the DEER measurement, leading to an underestimation of NV center concentrations^{29,30}. Secondly, this method becomes invalid if the NV center ensemble exhibits a preferential orientation⁴⁵. Moreover, some samples deviate from the exponential decay predicted by mean-field theory (e.g., sample C3 discussed in Section II E).

To address this limitation, an alternative method utilizing pulse sequences for Hamiltonian engineering is proposed. The sequences are designed to ensure that the effective Hamiltonian contains exclusively the NV-NV interaction term, which can be used to determine the NV-NV interaction strength by measuring the decay rate corresponding to the specific effective Hamiltonian^{46,47}. In theory, dynamic decoupling sequences consisting solely of π pulses can fulfill the requirement, and two approaches are available for their implementation. In the first approach, the π pulse interval time τ is fixed and kept sufficiently short to satisfy the approximation conditions of the Average Hamiltonian Theory (AHT), while the repetition number N is gradually increased to measure the T_2 decay time, with only the NV-NV interactions retained. Alternatively, in the second approach, τ is increased with a fixed N to determine the interaction strength, provided that N is sufficiently large and τ remains short enough to meet the AHT approximation conditions. In our experiments, we adopted the second approach to see the decays with fixed interaction cycles.

To ensure that the effective Hamiltonian contains only the NV-NV interaction term, it is crucial to choose a sequence capable of canceling multiple noise components, including those introduced by the DC disorder, AC disorder, finite pulse durations, pulse errors, and other sources. A series of simulations confirm that the XY8 and XY16 sequences are sufficiently robust against the above noise (see the Supplementary), leading to the selection of the XY sequence for the experiment, as depicted in Fig. 3c. The simulations also suggest a practical approach to ensure that N is sufficiently large to satisfy the conditions of Average Hamiltonian Theory (AHT) without prior knowledge. This involves performing several measurements with different values of N . When the measured decay time no longer changes with N , the saturated T_2 can be attributed to the effective Hamiltonian containing only the NV-NV interaction term. For the example sample, as shown in Fig. 3c–e, the decoherence rate saturates at $\Gamma_2 = 3\text{kHz}$ when the repetition number in the XY8 sequence is sufficiently large. Consequently, $\Gamma_{\text{NV-NV}}$ is determined to be 3kHz, corresponding to an NV concentration of approximately 0.17ppm.

Interestingly, the decay rate increases with N in the simulations but decreases in the experiments. In the simulations, higher-order terms in the Magnus expansion of the effective Hamiltonian obscure part of the NV-NV interaction strength. As the repetition number N increases, the effective Hamiltonian approaches the first-order term, recovering the full strength of the NV-NV interaction. Consequently, the decay rates measured using the XY8- N sequence increase with N in the simulations. However, in the experiments, neglected AC noise has a greater impact on the decay rate than the discrepancies caused by higher-order terms observed in the simulations. Sequences with larger repetition numbers N exhibit narrower bandwidths, effectively filtering out AC noise. As a result, the measured decoherence time increases with N , as shown in Fig. 3d and e. In either case, $\Gamma_{\text{NV-NV}}$ can be reliably estimated using a large repetition number N in the XY8- N or XY16- N sequence.

It is important to note that due to the Γ_1 limit, the detectable NV-NV interaction strength must exceed 0.1kHz, corresponding to an NV concentration of approximately 10 ppb. For such samples, Comparing the fluorescence intensity against a reference sample is an effective way to determine the NV concentration in this regime.

12 samples results

Using the presented methods, the dephasing characteristics of two groups of diamonds are analyzed: six samples grown using the high-pressure-high-temperature (HPHT) method (labeled H1-H6) and five samples grown using the chemical vapor deposition (CVD) method (labeled C1-C5). The initial nitrogen concentrations of the samples ranged from approximately 1 ppm to 30 ppm. The samples were irradiated and annealed under various conditions to optimize the conversion rate of the NV centers (details in the Methods). The results of the dephasing measurements are summarized in Table 1. The example sample described in Section II corresponds to H2 in Table 1. The longest $T_2^* = 11.8\mu\text{s}$ was measured with Sample C1, of which the estimated NV center concentration and the strain are the lowest among

Table 1 | Summary of measured decay rates

No.	Γ_2^* (kHz)	Γ_2 (kHz)	$\Gamma_{DQ/2}$ (kHz)	Γ_{elec} (kHz)	Γ_{strain} (kHz)	Γ_{C13} (kHz)	Γ_{NV-NV} (kHz)
H1	165(1)137(1.5)	4.5	125	2.9	34.6	~30	2
H2	129(1)117(1.2)	10	108	4.4	44.6	~30	3
H3	581	30.0	595	6.5	34.5	~5	5
H4	385	32.0	156	7.2	160.8	~5	6.6
H5	741	109.0	405	11.8	253.2	~5	13.3
H6	2800	625.0	1720	25.5	274.5	~5	62
C1	96(1)85(1.3)	4.2	86	2.3	30.6	~1	1.7
C2	167	8.0	77.5	3.5	88.5	~1	2.1
C3	800	15(1) 27(0.5)	96	6.2	1273.8	~1	3
C4	714	70.0	481	19	272	~1	20
C5	555	83.0	277	—	363.0	~1	22

the samples. Most samples exhibited a single exponential decay in the T_2^* measurements, except for a few with relatively long T_2^* values, namely H1, H2, and C1. A stretched exponential function was used to fit their T_2^* decay curves. The stretch factors are noted in parentheses in the table, and the dephasing rates obtained by forcing a single exponential decay fit are also reported.

To visualize the results, we plot different decay rates as a function of the NV center concentration, as shown in Fig. 4. The NV center concentrations of the samples were determined by measuring the NV-NV interactions, as described in Section II D. Since the strain distribution in diamonds strongly depends on the crystal growth process, Γ_{strain} is expected to be independent of the NV center concentration, which is shown in Fig. 4b. Γ_{elec} is plotted in Fig. 4a, which is much smaller than the inhomogeneous strain, proving that the S_z^2 term in \mathcal{H}_{NV} is primarily induced by the inhomogeneous strain rather than the electric field. Interestingly, Γ_{elec} exhibits a strong correlation with the concentration of NV centers. These results confirm that the electric field noise in diamonds is mostly induced by NV centers and their associated electron donors, consistent with Ref. 31. The predicted scaling factor of Γ_{elec} with [NV] is 11.2 kHz/ppm^{2/3}, as indicated by the green line in the figure. Furthermore, the results suggest that the upper limit of the NV concentration can be estimated from electric field noise measurements.

As described in Section II D, the dephasing rate Γ_2^* can be approximated as $\Gamma_{DQ/2} + \Gamma_{S_z^2}$. To evaluate this approximation, Fig. 4c plots the ratio $(\Gamma_{DQ/2} + \Gamma_{S_z^2})/\Gamma_2^*$. Most ratios fall within the 20% error margin, except for Sample C3, where Γ_2 is better fitted with a stretch factor of $p = 0.5$. This can be attributed to the high strain-induced decay rate in this sample. The results suggest that the independent-noise-source summation model generally describes dephasing behavior, but may oversimplify interactions between different noise sources, such as magnetic field noise competing with strain or electric field noise, as discussed in ref. 48.

The Hahn-echo measurements of Γ_2 , shown with a linear fit in Fig. 4d, reveal a strong correlation with the concentration of NV centers. Γ_2 is mainly contributed by: 1. NV-NV interactions, and 2. AC components of the spin bath induced by the P1 centers. Both sources contribute linearly to the decay rates, depending on their concentrations. With similar conversion efficiencies from the P1 centers to the NV centers for all samples, the density of the NV centers, the initial [N], and the residual concentration of the P1 centers should be correlated (Sample details are provided in the methods), which leads to the correlations observed in Fig. 4d. Small deviations from the fit for a few samples can be attributed to the variation of the conversion efficiencies (details in the methods).

Since the sensitivity per volume of DC diamond magnetometry directly depends on Γ_2^* and the concentration of the NV centers, the data are plotted in Fig. 4f. As shown, the best-performing samples can achieve a T_2^* of up to approximately 608 kHz/ppm. Based on the current results, we now consider

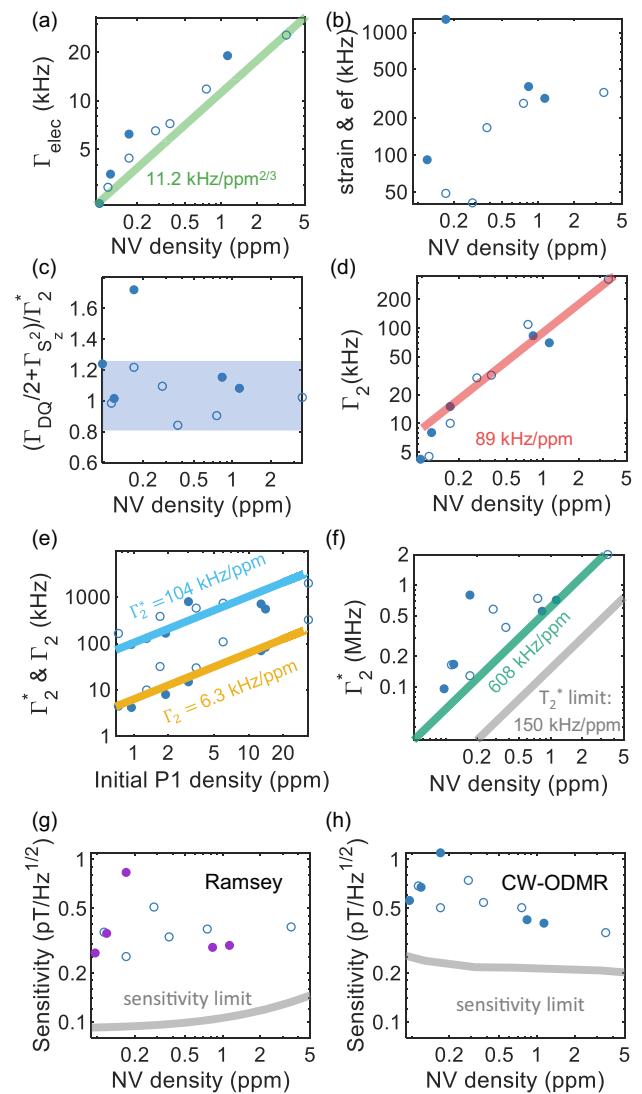


Fig. 4 | Characterization results from 11 diamond samples, where solid and hollow markers represent CVD- and HPHT-grown diamonds, respectively. **a** Decay rates induced by intrinsic electric field noise as a function of NV concentration, with the line showing the theoretical lower bound. **b** Strain and electric field induced dephasing rates. **c** Ratio between Γ_2^* and $\Gamma_{DQ/2} + \Gamma_{S_z^2}$ (sum of dipolar-induced and S_z^2 -related decay rates), where the shaded area represents deviations within 20%. **d** Γ_2 measured using Hahn-Echo sequence, with the red line showing the fitted linear relationship. **e** Relation between dephasing rate and initial nitrogen concentration. **f** Γ_2^* measurements with an estimated lower bound achievable through strain noise elimination. Calculated sensitivities based on measured Γ_2^* values and theoretical limits using **(g)** Ramsey method and **(h)** CWODMR.

how to further enhance $T_2^* \cdot N$. Given that all our samples underwent relatively thorough irradiation and annealing, a significant portion of the P1 centers is converted into N^+ , NV^0 , and NV^- (as well as possibly other centers such as NVH), as discussed in Section II C. Due to the hyperfine interactions and the existence of four crystallographic NV axes, both N^+ and NV^0 do not contribute to spin bath noise. Thus, a significant reduction of [P1] should lead to an improvement in T_2^* in theory, and the irradiation and annealing processes does not introduce additional dephasing sources.

To investigate this, we analyzed the dependence of T_2 and T_2^* on the initial nitrogen concentration in Fig. 4e. In these figures, we also plot the theoretical relations between T_2 , T_2^* , and [P1] (when the P1 centers dominate, i.e., without irradiation and annealing), as reported in ref. 26. Interestingly, the results of the irradiated and annealed samples still reasonably

follow the same trend with respect to the initial [P1]. It suggests that irradiation and annealing proportionally introduce other dephasing sources. A key candidate could be the vacancy clusters, which may contain many unpaired electrons—a possibility also hinted at in our DEER spectra. This underscores the need to explore more efficient irradiation and annealing protocols.

Furthermore, techniques such as double quantum (DQ) sensing combined with spin bath driving can be employed to mitigate the effects of strain and spin bath. This approach has been successfully demonstrated in samples without irradiation and annealing, yielding multiple-fold improvements. However, in irradiated and annealed samples, the significantly reduced [P1] limits the effectiveness of spin bath driving. In ref. 49, additional free electrons were driven to achieve an improvement of 2 times. When NV centers themselves become the dominant source of decoherence, pulse sequences such as WAHUA, which is designed to suppress NV-NV dipolar interactions, can be applied to further enhance T_2^* . Therefore, we estimate that T_2^* can be improved by at least a factor of 4 by combining the DQ technique with the bath-driving technique, reaching around 150 kHz/ppm, as indicated by the light gray line in Fig. 4f.

Finally, we evaluate the magnetic field sensitivity achievable by the samples according to their dephasing properties. Ramsey and continuous-wave ODMR are the two commonly used methods for DC magnetic field sensing. The maximum fluorescence photon number is assumed to scale linearly with NV density. This assumption, along with T_2^* and the estimated NV concentrations, is used to calculate the shot noise limits based on the Ramsey method¹⁷. For CW-ODMR, a five-level rate equation model is applied to determine the sensitivity limit⁵⁰. In the simulations, a volume of 0.04 mm³ was set for all diamonds. The results are shown in Fig. 4g and h. In addition, the optimal sensitivity limits are plotted for both Ramsey and CWODMR. The limits are derived from the optimal relationship between T_2^* and the density of the NV centers (gray line in Fig. 4f).

Understanding the dephasing characteristics of the NV centers provides a pathway to improve sensitivity by extending T_2^* . Improving the dephasing times highly depends on both the growth process and after-growth-treatments of diamonds. Low-strain diamonds, typically produced using the HPHT technique, are particularly critical. Recently, advances in the CVD method have enabled the growth of low-strain diamonds by using high quality HPHT diamonds as substrates, as demonstrated by samples C1 and C2 in Table 1. Moreover, techniques that suppress specific dephasing sources are essential for advancing NV center magnetometry. For instance, the double-quantum manipulation technique combined with bath driving effectively suppresses both strain and spin bath noises from the P1 centers³⁵. Residual dephasing from NV-NV interactions can also be mitigated using dipole-dipole decoupling sequences, such as WAHUA and MREV8 sequences, which suppress the NV-NV interaction term in the effective Hamiltonian⁵¹. Experimentally, the DC sensitivity determined by the T_2^* is a few pT/ $\sqrt{\text{Hz}}$ for the 0.04mm³ diamond. This is still an order of magnitude away from the shot-noise limit. This discrepancy is primarily attributed to technical noise, such as laser noise, which is challenging to reduce further at the current stage. Thus, extending T_2^* through advanced techniques represents the most effective approach to enhance DC sensitivity. Unraveling the dephasing mechanisms of each sample enables the combination of multiple noise-decoupling techniques to further extend T_2^* .

Discussions

This work proposes and demonstrates multiple techniques to characterize and understand the dephasing mechanisms of NV center ensembles in diamonds. Diamonds grown and processed under different conditions were systematically studied. Dephasing sources are classified into several groups, and their corresponding decay rates are measured. Intrinsic strain and electric-field noise were precisely characterized using a combination of the strain-CPMG sequence and the zero-field ODMR spectrum. The decay rate from dipolar noise, primarily due to the spin bath from P1 centers, is measured by applying the duration-sweep DEER sequence for the samples with low paramagnetic defect concentrations. For NV-NV interactions, we

employed XY8-*N* sequences to resolve weak couplings and infer NV concentrations. More importantly, understanding the dephasing sources for a given sample provides guidance for selecting specific techniques to suppress the dominant noises, thereby improving the DC magnetic-field sensitivity. The sensitivity limit that could be achieved with the samples used in this work is discussed. In addition to the techniques discussed, further improvements are expected with advancements in diamond growth technology. For example, phosphorus-doped n-type diamond demonstrates a 1 ms dephasing time for single NV centers⁵². One-to-two-order improvement in T_2^* can be expected. By improving the DC magnetic field sensitivity to the sub-pT level, diamond magnetometry can be competitive with the state-of-the-art high-sensitivity quantum magnetometers while maintaining the sub-mm spatial resolution.

Methods

Setup information

The experimental measurements were performed using a custom-built confocal-like microscopy setup but without a pinhole. We employed a 20 ×, 0.4 NA long working distance objective (12 mm), resulting in an excitation and detection volume of approximately 1 μm laterally and 40 μm axially. Since the detection volume can affect the influence of both the B_0 gradient and strain distribution on the resulting T_2^* , we also conducted control measurements on samples H1 and H2 using wide-field illumination that covered the entire diamond (0.5 × 0.5 × 0.5mm³). The results showed no observable differences, indicating that the current detection volume is sufficiently “macroscopic.” Therefore, the T_2^* values measured under this setup can be reliably used for estimating the sensitivity of bulk-based magnetic field measurements. The optical excitation system consists of a high-power 532 nm laser (Lighthouse) for NV center excitation, while the fluorescence detection system employs an avalanche photodiode (Thorlabs APD130A2M) coupled with a high-speed data acquisition card (Spectrum M4i.4421) for signal recording. The microwave (MW) driving field was generated using a combination of RF sources: an Apsin Anapico 4010 serving as the local oscillator, mixed with signals from an arbitrary wave generator (Spectrum DN2.6631), and an additional RF source (Apsin Anapico 3000) specifically for DQ and Strain sequence generation. The precise timing control of laser excitation, fluorescence detection, and RF driving was achieved using a pulse generator (Spincore PulseBlasterESR-PRO).

Preparation of diamond samples

This section presents the growth conditions, post-treatment procedures, and typical measurement data for the samples listed in Table 1. Detailed growth and treatment parameters are summarized in Table 2. Sample C5

Table 2 | Sample characteristics and treatment details

No.	[¹² C] (%)	Electrons Irradiation	Annealing	Initial Nitrogen
H1	99.970	2 MeV, 2×10^{17} e/cm ² × 2	1000 °C 2 h	0.74 ppm
H2	99.970	2 MeV, 7×10^{17} e/cm ²	1000 °C 2 h	1.3 ppm
H3	99.995	2 MeV, 1×10^{17} e/cm ² × 2	1000 °C 2 h × 2	3.5 ppm
H4	99.995	2 MeV, 1.5×10^{17} e/cm ² + 2 MeV, 0.5×10^{17} e/cm ²	1000 °C 2 h × 2	1.7 ppm
H5	99.995	2 MeV, 1×10^{17} e/cm ² × 3	1000 °C 2 h × 3	6 ppm
H6	99.995	2 MeV, 1×10^{17} e/cm ² × 5	1000 °C 2 h × 5	33 ppm
C1	99.999	1 MeV, 4.8×10^{17} e/cm ²	800 °C 10 h	0.96 ppm
C2	99.999	1 MeV, 3.4×10^{17} e/cm ²	+1200 °C 1 h	1.9 ppm
C3	99.999	1 MeV, 6.9×10^{17} e/cm ²		3.0 ppm
C4	99.999	4.5 MeV, 5.8×10^{17} e/cm ²		12.8 ppm
C5	99.999	6 MeV, 6.0×10^{17} e/cm ²		14 ppm

Note: ¹⁵N is used in the growth of sample C5, while the other samples are grown with ¹⁴N.

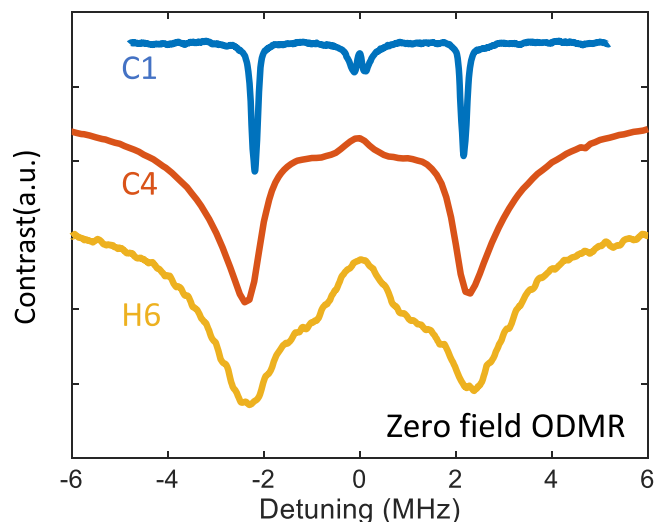


Fig. 5 | Zero-field ODMR measurements on three different samples.

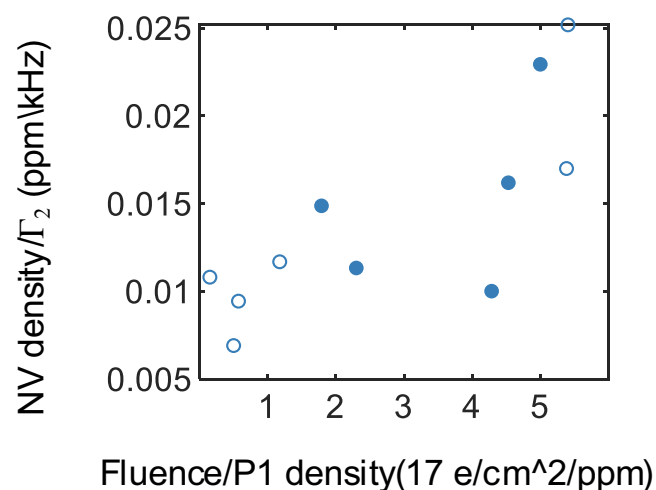


Fig. 6 | **Parameter relation:** 1. Ratio between the NV center density and Γ_2 , 2. Ratio between the electron irradiation dose and the P1 center density.

contains ^{15}N rather than ^{14}N atoms and lacks nuclear spin levels with spin = 0, preventing the observation of true zero-ODMR signals. Consequently, the zero-field ODMR technique cannot differentiate between electric field and strain noise contributions in this sample. Figure 5 presents representative zero-field ODMR measurements from three samples, selected to demonstrate the progression of increasing electric-field noise.

More details about HPHT samples are as follows. H1 and H2 were grown at 6.1 GPa and 1430 °C by using a Fe-Al metal solvent. As the ^{12}C -enriched solid carbon sources, CVD powder and ^{12}C -enriched pyrolytic carbon powder fabricated from ^{12}C -enriched methane were used for H1 and H2, respectively. H3-H6 were grown at 5.5 GPa and 1350 °C using Fe-Co-Ti solvent and ^{12}C -enriched solid carbon source obtained by pyrolysis of 99.999 % ^{12}C -enriched methane. The isotopic abundance ratio of the grown crystals was determined by SIMS measurement. Nitrogen concentration was controlled by changing the amount of nitrogen getter. H1 was irradiated at 450 °C by irradiating the crystal on a platinum plate in a sealed silica-glass tube. After two cycles of irradiation, H1 was annealed at 1000 °C for 2 h under vacuum. Samples H2, H3, H4, H5, and H6 were irradiated with 2 MeV electrons at room temperature. Except for H2, the samples were irradiated in multiple steps and annealed (1000 °C for 2 h under vacuum) after each irradiation, as shown in Table 2.

Here we analyze the observed linear relationship between NV center concentration and Γ_2 , and explain the deviations observed in certain samples. Previous studies on diamonds with low P1-to-NV conversion rates have identified P1 centers as the primary decoherence source for T_2 ^{26,53,54}. These studies established a decoherence contribution factor of 6.3 kHz/ppm for P1 centers²⁶. For cases where NV-NV interactions dominate the decoherence process, the contribution factor is 20.6 kHz/ppm¹⁷. In our samples, which exhibit high P1-to-NV conversion efficiencies, Γ_2 receives contributions from both P1 and NV centers. Moreover, the observed deviations from linearity can be attributed to varying conversion efficiency from P1 to NV centers. Since the conversion efficiency is directly related to electron irradiation, we verified our interpretation by examining two key parameters: the ratio of NV center density to Γ_2 , and the ratio of electron irradiation dose to initial P1 center density. Both parameters should be proportional to the conversion efficiency, and indeed, as shown in Fig. 6, they exhibit a linear relationship. The electron irradiation doses and initial P1 center concentrations used in this analysis are provided in Table 2.

Data availability

All data included in this study are available from the corresponding authors upon reasonable request.

Code availability

All code included in this study are available from the corresponding authors upon reasonable request.

Received: 15 June 2025; Accepted: 21 February 2026;

Published online: 12 March 2026

References

- Balasubramanian, G. et al. Nanoscale imaging magnetometry with diamond spins under ambient conditions. *Nature* **455**, 648 (2008).
- Koehl, W. F., Buckley, B. B., Heremans, F. J., Calusine, G. & Awschalom, D. D. Room temperature coherent control of defect spin qubits in silicon carbide. *Nature* **479**, 84–87 (2011).
- Atatüre, M., Englund, D., Vamivakas, N., Lee, S.-Y. & Wrachtrup, J. Material platforms for spin-based photonic quantum technologies. *Nat. Rev. Mater.* **3**, 38–51 (2018).
- Hsieh, S. et al. Imaging stress and magnetism at high pressures using a nanoscale quantum sensor. *Science* **366**, 1349–1354 (2019).
- Dolde, F. et al. Electric-field sensing using single diamond spins. *Nat. Phys.* **7**, 459–463 (2011).
- Maletinsky, P. et al. A robust scanning diamond sensor for nanoscale imaging with single nitrogen-vacancy centres. *Nat. Nanotechnol.* **7**, 320–324 (2012).
- Abobeih, M. et al. Fault-tolerant operation of a logical qubit in a diamond quantum processor. *Nature* **606**, 884–889 (2022).
- Boto, E. et al. Moving magnetoencephalography towards real-world applications with a wearable system. *Nature* **555**, 657–661 (2018).
- Shi, F. et al. Single-protein spin resonance spectroscopy under ambient conditions. *Science* **347**, 1135–1138 (2015).
- Song, T. et al. Direct visualization of magnetic domains and moiré magnetism in twisted 2d magnets. *Science* **374**, 1140–1144 (2021).
- Du, J., Shi, F., Kong, X., Jelezko, F. & Wrachtrup, J. Single-molecule scale magnetic resonance spectroscopy using quantum diamond sensors. *Rev. Mod. Phys.* **96**, 025001 (2024).
- Xie, Y.-M. & Nagaosa, N. Probing loop currents and collective modes of charge density waves in kagome materials with nv centers. *npj Quantum Mater.* **10**, 64 (2025).
- Barry, J. F. et al. Sensitive ac and dc magnetometry with nitrogen-vacancy-center ensembles in diamond. *Phys. Rev. Appl.* **22**, 044069 (2024).
- Levine, E. V. et al. Principles and techniques of the quantum diamond microscope. *Nanophotonics* **8**, 1945–1973 (2019).

15. Huang, Y. et al. New constraints on exotic spin-spin-velocity-dependent interactions with solid-state quantum sensors. *Phys. Rev. Lett.* **132**, 180801 (2024).
16. Zhang, C. et al. Optimizing nv magnetometry for magnetoneurography and magnetomyography applications. *Front. Neurosci.* **16**, 2340 (2022).
17. Barry, J. F. et al. Sensitivity optimization for nv-diamond magnetometry. *Rev. Mod. Phys.* **92**, 015004 (2020).
18. Edmonds, A. M. et al. Characterisation of cvd diamond with high concentrations of nitrogen for magnetic-field sensing applications. *Mater. Quantum Technol.* **1**, 025001 (2021).
19. Allred, J., Lyman, R., Kornack, T. & Romalis, M. V. High-sensitivity atomic magnetometer unaffected by spin-exchange relaxation. *Phys. Rev. Lett.* **89**, 130801 (2002).
20. Luo, T. et al. Creation of nitrogen-vacancy centers in chemical vapor deposition diamond for sensing applications. *N. J. Phys.* **24**, 033030 (2022).
21. Kucsko, G. et al. Critical thermalization of a disordered dipolar spin system in diamond. *Phys. Rev. Lett.* **121**, 023601 (2018).
22. Choi, J. et al. Robust dynamic hamiltonian engineering of many-body spin systems. *Phys. Rev. X* **10**, 031002 (2020).
23. Abanin, D. A., Altman, E., Bloch, I. & Serbyn, M. Colloquium: Many-body localization, thermalization, and entanglement. *Rev. Mod. Phys.* **91**, 021001 (2019).
24. Hymas, K. et al. Discriminating ferrotoroidic from antiferrotoroidic ground states using a 3d quantum spin sensor. *npj Quantum Mater.* **9**, 106 (2024).
25. Ciccarino, C. J. et al. Strong spin-orbit quenching via the product jahn-teller effect in neutral group iv qubits in diamond. *npj Quantum Mater.* **5**, 75 (2020).
26. Bauch, E. et al. Decoherence of ensembles of nitrogen-vacancy centers in diamond. *Phys. Rev. B* **102**, 134210 (2020).
27. Dobrovitski, V. V., Feiguin, A. E., Awschalom, D. D. & Hanson, R. Decoherence dynamics of a single spin versus spin ensemble. *Phys. Rev. B* **77**, 245212 (2008).
28. Wang, Y. *Using spins in diamond for quantum technologies*. Ph.D. thesis, Delft University of Technology (2023).
29. Eichhorn, T. R., McLellan, C. A. & Bleszynski Jayich, A. C. Optimizing the formation of depth-confined nitrogen vacancy center spin ensembles in diamond for quantum sensing. *Phys. Rev. Mater.* **3**, 113802 (2019).
30. Li, S. et al. Determination of local defect density in diamond by double electron-electron resonance. *Phys. Rev. B* **104**, 094307 (2021).
31. Mittiga, T. et al. Imaging the local charge environment of nitrogen-vacancy centers in diamond. *Phys. Rev. Lett.* **121**, 246402 (2018).
32. Marshall, M. C. et al. High-precision mapping of diamond crystal strain using quantum interferometry. *Phys. Rev. Appl.* **17**, 024041 (2022).
33. Balasubramanian, P. et al. Dc magnetometry with engineered nitrogen-vacancy spin ensembles in diamond. *Nano Lett.* **19**, 6681–6686 (2019).
34. Cambria, M. C. et al. State-dependent phonon-limited spin relaxation of nitrogen-vacancy centers. *Phys. Rev. Res.* **3**, 013123 (2021).
35. Bauch, E. et al. Ultralong dephasing times in solid-state spin ensembles via quantum control. *Phys. Rev. X* **8**, 031025 (2018).
36. Abragam, A. *The Principles of Nuclear Magnetism* vol. 32 (Oxford University Press, 1961).
37. Rubinas, O. R. et al. Optimization of the double electron-electron resonance for c-centers in diamond. *Phys. status solidi (RRL) - Rapid Res. Lett.* **16**, 2100561 (2022).
38. Degen, M. et al. Entanglement of dark electron-nuclear spin defects in diamond. *Nat. Commun.* **12**, 1–10 (2021).
39. Grinolds, M. et al. Subnanometre resolution in three-dimensional magnetic resonance imaging of individual dark spins. *Nat. Nanotechnol.* **9**, 279–284 (2014).
40. Findler, C. et al. Detecting nitrogen-vacancy-hydrogen centers on the nanoscale using nitrogen-vacancy centers in diamond. *Phys. Rev. Mater.* **8**, 026203 (2024).
41. Wong, K. C. et al. Microscopic study of optically stable coherent color centers in diamond generated by high-temperature annealing. *Phys. Rev. Appl.* **18**, 024044 (2022).
42. Knowles, H. S., Kara, D. M. & Atatüre, M. Observing bulk diamond spin coherence in high-purity nanodiamonds. *Nat. Mater.* **13**, 21–25 (2014).
43. De Lange, G. et al. Controlling the quantum dynamics of a mesoscopic spin bath in diamond. *Sci. Rep.* **2**, 1–5 (2012).
44. Joos, M., Bluvstein, D., Lyu, Y., Weld, D. & Bleszynski Jayich, A. Protecting qubit coherence by spectrally engineered driving of the spin environment. *npj Quantum Inf.* **8**, 1–5 (2022).
45. Michl, J. et al. Perfect alignment and preferential orientation of nitrogen-vacancy centers during chemical vapor deposition diamond growth on (111) surfaces. *Applied Physics Letters* **104** (2014).
46. Schenken, W. K. et al. Long-lived coherences in strongly interacting spin ensembles. *arXiv preprint arXiv:2309.15444* (2023).
47. He, G. et al. Quasi-floquet prethermalization in a disordered dipolar spin ensemble in diamond. *Phys. Rev. Lett.* **131**, 130401 (2023).
48. Jamonneau, P. et al. Competition between electric field and magnetic field noise in the decoherence of a single spin in diamond. *Phys. Rev. B* **93**, 024305 (2016).
49. Tang, J. et al. Quantum diamond microscope for dynamic imaging of magnetic fields. *AVS Quantum Science* **5** (2023).
50. Zhang, C. et al. Diamond magnetometry and gradiometry towards subpicotesla dc field measurement. *Phys. Rev. Appl.* **15**, 064075 (2021).
51. Aslam, N. et al. Nanoscale nuclear magnetic resonance with chemical resolution. *Science* **357**, 67–71 (2017).
52. Herbschleb, E. et al. Ultra-long coherence times amongst room-temperature solid-state spins. *Nat. Commun.* **10**, 3766 (2019).
53. Yang, W. & Liu, R.-B. Quantum many-body theory of qubit decoherence in a finite-size spin bath. ii. ensemble dynamics. *Phys. Rev. B* **79**, 115320 (2009).
54. Park, H., Lee, J., Han, S., Oh, S. & Seo, H. Decoherence of nitrogen-vacancy spin ensembles in a nitrogen electron-nuclear spin bath in diamond. *npj Quantum Inf.* **8**, 1–6 (2022).

Acknowledgements

Jixing Zhang and Cheuk Kit Cheung contributed equally to this work as co-first authors. We acknowledge the financial support by EU via project AMADEUS, the BMBF via projects DiaQnos and NeuroQ as well as QHMI and the DFG via GRK 2642. In addition, C.Z. acknowledges the financial support by the NSFC via Grant 62473058. The work was performed in part under the collaboration agreement among University of Tsukuba, University of Ulm and University of Stuttgart.

Author contributions

J.W. conceived and supervised the project. J.Z., C.Z., C.k.C., M.K., and M. Benke conducted the experiments. J.Z. and M. Brossaud. conducted the simulations. J.Z., Y.W., R.P., J.A., E.C., and C.T.S. contributed to the theory. A.D., A.E., M.M., K.N., H.S., S.O., J.I. prepared the diamond samples. All authors have contributed to the interpretation of the data and the drafting as well as the revision of the manuscript.

Funding

Open Access funding enabled and organized by Projekt DEAL.

Competing interests

The authors declare no competing interests.

Additional information

Supplementary information The online version contains supplementary material available at <https://doi.org/10.1038/s41535-026-00869-5>.

Correspondence and requests for materials should be addressed to Jixing Zhang or Chen Zhang.

Reprints and permissions information is available at <http://www.nature.com/reprints>

Publisher's note Springer Nature remains neutral with regard to jurisdictional claims in published maps and institutional affiliations.

Open Access This article is licensed under a Creative Commons Attribution 4.0 International License, which permits use, sharing, adaptation, distribution and reproduction in any medium or format, as long as you give appropriate credit to the original author(s) and the source, provide a link to the Creative Commons licence, and indicate if changes were made. The images or other third party material in this article are included in the article's Creative Commons licence, unless indicated otherwise in a credit line to the material. If material is not included in the article's Creative Commons licence and your intended use is not permitted by statutory regulation or exceeds the permitted use, you will need to obtain permission directly from the copyright holder. To view a copy of this licence, visit <http://creativecommons.org/licenses/by/4.0/>.

© The Author(s) 2026